Integration of fiber optic-particle plasmon resonance biosensor with microfluidic chip

Wei-Ting Hsu [a], Wen-Hsin Hsieh [b,c], Shu-Fang Cheng [a], Chung-Ping Jen [b,c], Chao-Ching Wu [a], Cheng-Han Li [a], Chia-Yu Lee [c], Wan-Yun Li [c], Lai-Kwan Chau [a,c,*], Chang-Yue Chiang [a], Shaw-Ruey Lyu [d]

[a] Department of Chemistry and Biochemistry, National Chung Cheng University, Chiayi 62102, Taiwan
[b] Department of Mechanical Engineering, National Chung Cheng University, Chiayi 62102, Taiwan
[c] Center for Nano Bio-Detection, National Chung Cheng University, Chiayi 62102, Taiwan
[d] Joint Center, Buddhist Dalin Tzu Chi General Hospital, Chiayi 62247, Taiwan

ABSTRACT

This article reports the integration of the fiber optic-particle plasmon resonance (FO-PPR) biosensor with a microfluidic chip to reduce response time and improve detection limit. The microfluidic chip made of poly(methyl methacrylate) had a flow-channel of dimensions $4.0\,cm \times 900\,\mu m \times 900\,\mu m$. A partially unclad optical fiber with gold or silver nanoparticles on the core surface was placed within the flow-channel, where the volume of the flow space was about $14\,\mu L$. Results using sucrose solutions of various refractive indexes show that the refractive index resolution improves by 2.4-fold in the microfluidic system. The microfluidic chip is capable of delivering a precise amount of biological samples to the detection area without sample dilution. Several receptor/analyte pairs were chosen to examine the biosensing capability of the integrated platform: biotin/streptavidin, biotin/anti-biotin, DNP/anti-DNP, OVA/anti-OVA, and anti-MMP-3/MMP-3. Results show that the response time to achieve equilibrium can be shortened from several thousand seconds in a conventional liquid cell to several hundred seconds in a microfluidic flow-cell. In addition, the detection limit also improves by about one order of magnitude. Furthermore, the normalization by using the relative change of transmission response as the sensor output alleviate the demand on precise optical alignment, resulting in reasonably good chip-to-chip measurement reproducibility.

© 2011 Elsevier B.V. All rights reserved.

1. Introduction

The performance of many biosensors is limited by the rate at which an analyte molecule is transported to a surface-immobilized recognition molecule [1,2]. When this recognition process is diffusion-limited, the sensor's detection limit and response time can be determined by analyte mass transport. Hence, ways to improve mass transport are desirable in biosensing systems. Microfluidic flow-cell has several characteristic features different from bulk scale, for example, short diffusion distance, high interface-to-volume ratio, and small heat capacity [3]. These characteristics in the microfluidic flow-cell are keys to improving biosensor performance characteristics, such as response time [4], sample capture fraction [5], and consumption of samples and reagents. Especially, to control molecular transport in a sensor cell,

miniaturization of the sensor flow-cell is expected to reduce the response time since molecular transportation time is proportional to the square of the scale [3].

The recent progress in high sensitivity optical transducers combined with the excellent specificity, affinity, and versatility of bio-molecular interactions has driven the development of a wide variety of optical biosensors with applications in diverse fields including clinical diagnosis, food and agricultural analysis, and environmental monitoring. The most extensively employed optical biosensors are those based on surface plasmon resonance (SPR) sensors using thin gold films [6]. Of which, integration of some SPR sensors with microfluidics has been reported [7,8]. Moreover, the SPR sensing technique has been extended to microarray imaging [7,9,10] and many interesting biosensing applications have been demonstrated [11–14]. Unfortunately, prism or grating-based SPR sensors require bulky and expensive optical components and hence are difficult to be miniaturized. Consequently, fiber-optic-based SPR sensors with either wavelength or intensity modulation have been developed [15–17]. However, the operation range of fiber-optic SPR sensor is limited by the phase matching require-

* Corresponding author at: Department of Chemistry and Biochemistry, National Chung Cheng University, Chiayi 62102, Taiwan. Tel.: +886 5 2720411x66411; fax: +886 5 2721040.
E-mail address: chelkc@ccu.edu.tw (L.-K. Chau).

ment [6]. As such, various approaches have been used to tune the resonant coupling in the refractive index range of aqueous samples [6,17].

Recently, scientific community has begun to explore alternative strategies for the development of new optical sensing platforms based on the extraordinary optical properties of noble metal nanoparticles [18–20]. These nanoparticles characteristically exhibit a strong extinction band that is not present in the spectrum of the bulk metal. The extinction band results when the incident photon frequency is resonant with the collective oscillation of the conduction electrons and is known as particle plasmon resonance (PPR), also known as localized surface plasmon resonance (LSPR). The extinction cross-section and peak wavelength of the PPR band are highly dependent on the local environment of the nanoparticle (i.e., refractive index of surrounding medium) [21–26], and furthermore, the binding events to those functionalized nanoparticles [26–31]. For such PPR sensors, the immobilized noble metal nanoparticles act as chromophores, while their interactions with analyte molecules will result in colorimetric changes. With a suitable receptor immobilized on the surface of the noble metal nanoparticles, the resulting PPR sensor can detect the corresponding analyte even if the analyte is spectroscopically silent in the UV–vis region. However, the signal-to-noise ratio for PPR sensors obtained by either the transmission mode with a single pass of light or reflection mode with a double pass of light through a monolayer of nanoparticles is not so high, as a result of the low absorbance of a monolayer of nanoparticles. The absorbance of such a monolayer can be enhanced by optical fiber sensing scheme [30,32,33] which is based on the absorption of the evanescent field via multiple total internal reflections. Therefore, with a suitable receptor immobilized on the surface of the noble metal nanoparticles, an analyte can be determined in real-time without the use of a labeled molecule [30,32–35], which is particularly attractive for chemical and biological sensing applications.

Although optical fibers are ideal media to guide light for the excitation of the plasmon resonance, the integration of optical fiber to other biosensor components raises some design concern [36]. This study demonstrates the feasibility of the integration of the fiber optic-particle plasmon resonance (FO-PPR) biosensor with microfluidic technology. As compared to the FO-PPR biosensor in a conventional liquid cell, the high surface to volume ratio of the microfluidic flow-cell enhances mass transport [37], resulting in improved biosensor performance characteristics such as shorter response time, better detection limit, and lower consumption of samples and reagents.

2. Experimental

2.1. Reagents and materials

Multimode plastic-clad silica optical fiber (model F-MBC) was purchased from Newport with core and cladding diameters of 400 and 430 μm, respectively. Poly(methyl methacrylate) (PMMA) for manufacturing microfluidic chip was purchased from Sheng-Yang Business. The following chemicals, n-hexadecyltrimethylammonium bromide (CTAB, Fluka), sodium borohydride (Lancaster), 3-(mercaptopropyl)-trimethoxysilane (MPTMS, Acros), sucrose (Osaka), 2-(4-(2-hydroxyethyl)-1-piperazinyl)-ethanesulfonic acid (HEPES, Fluka), 1-ethyl-3-(3-dimethylaminopropyl)-carbodiimide hydrochloride (EDC, Fluka), biotin (Aldrich), dinitrophenyl-epsilon-aminocaproic acid (DNP, ICN), streptavidin (Fluka), anti-biotin antibody (Sigma), anti-dinitrophenyl antibody (anti-DNP, Sigma), ovalbumin (OVA, Sigma–Aldrich) from chicken egg white, anti-OVA antibody (monoclonal anti-albumin chicken egg

clone OVA-14, Sigma–Aldrich), human matrix metalloproteinase-3 (MMP-3, Prospec), and anti-human MMP-3 antibody (anti-MMP-3, Thermo) were used as received. All aqueous solutions were prepared with water that had been purified by using a Millipore Milli-Q water purification system (Millipore) with a specific resistance of 18.2 MΩ cm. Solutions of various refractive indexes (1.342–1.403) were prepared by dissolving sucrose in purified water with a concentration between 6.8% and 41.7% [38].

2.2. Preparation of Au nanoparticles

Aqueous solution of hydrogen tetrachloroaurate (1.78 mL, 25.4 mM), chloroform (8.22 mL), and ethanol solution of CTAB (0.4 mL, 0.02 M) were mixed and stirred for 10 min to form a 4.52×10^{-4} M hydrogen tetrachloroaurate solution. Freshly prepared $NaBH_4$ ethanol solution (0.8 mL, 0.15 M) was added to the hydrogen tetrachloroaurate solution with vigorous stirring. After the solution was further stirred for 30 min, the ruby-colored organic phase was separated. Absorption spectra of the solution samples and immobilized noble metal nanoparticles on glass slides were obtained by using a Jusco V-570 spectrophotometer. A JEOL 1200 EX transmission election microscope (TEM) operating at 120 kV was used to obtain the images of the Au nanoparticles (AuNPs). Specimens for TEM were prepared by placing a sample on a copper grid and allowing it to dry. Histograms derived from TEM image analysis showed that the mean diameter of AuNPs was 15.9 ± 2.5 nm ($n = 500$).

2.3. Preparation of Ag nanoparticles

Following the procedures of a previous report [39], silver nitrate was used as the precursor to synthesize silver nanoparticles (AgNPs). Ethylene glycol was used as the solvent for silver nitrate and as the reducing agent. Polyvinylpyrrolidone (PVP) was used as the protecting agent. PVP (0.013 M) and $AgNO_3$ (0.032 M) were dissolved in 75 mL of ethylene glycol at room temperature. Then, the system was heated to 120 °C at a constant rate of $1 °C min^{-1}$, and the reaction was allowed to proceed for 22 h at this temperature. Afterward, each sample was cooled rapidly in a water bath until the system reached room temperature. TEM image analysis showed that the mean diameter of AgNPs was 31.6 ± 8.4 nm ($n = 444$).

2.4. Preparation of noble metal nanoparticles-modified optical fibers

For the optical fibers used as the FO-PPR sensor fibers, their distal ends were polished to an optically smooth surface to increase the transmission efficiency and 2 cm lengths of unclad portions were used. The unclad portion of the optical fibers was cleaned for 30 min in a bath consisting of 3 volumes of 30% H_2O_2 and 7 volumes of concentrated H_2SO_4. The clean unclad portions of the optical fibers were then submerged into vials of 1% solution of MPTMS in toluene. After 12 h, the optical fibers were rinsed with methanol and placed into an oven at 60 °C for 30 min to remove unbound monomers from the surface. After thorough rinsing and heating, the unclad portions of the optical fibers were immersed in a solution of noble metal nanoparticles for 12 h to form a self-assembled monolayer of noble metal nanoparticles on the core surface. Subsequently, the modified optical fibers were rinsed sequentially with water, methanol, and chloroform.

2.5. Immobilization of receptor onto nanoparticle surface

To functionalize DNP or biotin on the surface of noble metal nanoparticles on an optical fiber, a self-assembled monolayer (SAM) of cystamine was fist formed by injection of an aqueous

solution of cystamine dihydrochloride into the microfluidic sensing chip for 2 h at room temperature. The cystamine-modified nanoparticles were further functionalized with DNP or biotin by injection of a solution of HEPES, EDC, and the corresponding receptor molecule into a microfluidic sensor chip and allowed to react for 30 min at room temperature, then rinsed with water and air-dried at room temperature. To functionalize OVA or anti-MMP-3 on the noble metal nanoparticle surface, a procedure as previously described was followed [33].

2.6. Microfluidic channel design and chip manufacture

The microfluidic chip was produced by injection molding technique. The injected PMMA top plate with microfluidic channel and the PMMA bottom plate (see Fig. 1) both had a dimension of 4.0 cm (length) × 4.0 cm (width) × 0.2 cm (thickness). In order to accommodate the optical fiber which had a coating diameter of 730 μm, the microfluidic channel was fabricated with length, width and depth of 4 cm, 900 μm and 900 μm, respectively, and had a volume of about 32 μL. An inlet and an outlet on the top plate for sample introduction were connected to two small access holes and mechanically bored into the microfluidic channel. After the sensor fiber had been placed into the microfluidic channel on the top plate and caped with the bottom plate, the two PMMA plates were bonded by a thermal bonding process (heating the chip at 150 °C for 7 min and cooling the chip at room temperature) to produce the microfluidic sensor chip. The total length of the optical fiber was 8 cm and the unclad portion as the sensor zone in the middle segment was 2 cm. The free volume of the microfluidic channel was about 14 μL, when the microfluidic channel was occupied by an optical fiber. Samples and reagents can be injected by a syringe pump for functionalization or detection. Fig. 1 shows the components of the FO-PPR microfluidic sensor chip.

2.7. Principle of the FO-PPR biosensor

Optical fiber evanescent-wave absorption sensors are based on attenuated total reflection spectroscopy. This technique relies on the penetration of the evanescent-wave in the absorbing medium outside the fiber core and interacts with an analyte, whose distance from the fiber surface is generally smaller than the wavelength of the traveling light [40]. Since light propagates in optical fiber by virtue of multiple total internal reflections, the summation of each local evanescent-field results in a continuous evanescent-field at the waveguide surface immediately adjacent to the region occupied by a propagating mode. As a result, the overall sensitivity of the structure depends on the modes of light propagation in the fiber [41], the length of the fiber core exposed to the chromophores [42], and the chemical interaction between the analyte and the immobilized binding sites [43]. Hence, the low absorbance of a monolayer of noble metal nanoparticles can be enhanced by a fiber optic evanescent-wave sensing scheme [30]. Fiber optic evanescent-wave absorption measurements typically are performed by comparing the light intensity of a sensor immersed in an analyte solution (I_S) to the intensity of the sensor in a blank (I_0). Our sensor response in subsequent studies will be presented as ($I_0 - I_S$)/I_0 or $\Delta I/I_0$. In a sample of refractive index n_S different from that of a blank, n_0, the transmission response of the sensor fiber changes [29,32,33]. The plot of $\Delta I/I_0$ versus n_S has a linear relationship [33].

One parameter to characterize the performance of the class of refractive index-based sensors is the refractive index resolution (RIR), which is defined as the minimum change in refractive index unit (RIU) that can be resolved by the sensor. Operationally, the RIR in this study is the noise of the senor output which translates to the

change in bulk refractive index [6], where the noise is taken as the standard deviation of $\Delta I/I_0$ for 5 repetitive measurements.

2.8. Sensing system and measurements

As shown in Fig. 2, the sensor system consisted of a fiber optic light-emitting diode (LED) with a peak wavelength of 532 nm (model IF-E93, Industrial Fiber Optics, Inc.), a function generator (model GFG-8255A, Good will Instrument Co.) to modulate the LED output at a frequency of about 1 kHz, a lock-in amplifier (model 7225, Signal Recovery), a microfluidic FO-PPR sensor chip, and a photodiode (model 2001, New Focus).

The performance of receptor-functionalized FO-PPR sensors was examined by passing a sample into the microfluidic channel of a sensor chip. For these tests, the flow of a sample was stopped once the sample had filled the channel completely and the sensor responses were followed in real time. Typically, the sensor responses at several hundred seconds were used to construct a calibration graph. In this study, the detection limit and the quantification limit are defined as the sensor response ($\Delta I/I_0$) that yields a signal-to-noise ratio of 3 and 20, respectively, where the noise is taken as the standard deviation of $\Delta I/I_0$ for 5 repetitive measurements.

2.9. Preparation and analysis of synovial fluid samples

This study has been evaluated and approved by the ethics committee of Tzu Chi hospital. Informed consent was obtained from all patients participating in the study. The synovial fluids secreted from joint tissues of knees were collected by Tzu Chi hospital from patients suffering from osteoarthritis. The samples were stored at −80 °C until use. Each sample was diluted 25-fold and then a centrifugal filter device (Amicon Ultra-4, Millipore) was used to remove blood cells and proteins by centrifuging at 5000 rpm for 25 min. For FO-PPR sensing, a new anti-MMP-3 functionalized sensor chip was used for each sample. For enzyme-linked immunosorbent assay (ELISA), the measurements of MMP-3 were performed using an ELISA kit (Bioo Scientific), according to the manufacturer's instructions. Statistical analysis was performed using the InStat version 3.0 software (GraphPad Software). For the test of normality, the Kolmogorov-Smirnov test was used.

## 3. Results and discussion

3.1. Bioconjugation

Gold nanoparticles on glass slides were first used to optimize the bioconjugation processes by observing the spectral changes of a self-assembled monolayer of AuNPs on a glass slide before and after modification. As illustrated in Fig. 3, increases in peak absorbance were observed after modification of the gold nanoparticle surface with a monolayer of cystamine and then further reacted with biotin. Such spectral changes are consistent with the fact that the extinction spectra of AuNPs are sensitive to the refractive index of the surrounding environment. Also shown in Fig. 3, the monolayer of biotin-functionalized AuNPs in the presence of a sample of anti-biotin shows increase in peak absorbance. Such observations indicate that the bioconjugation process was successful.

3.2. Refractive index resolution

Using the same functionalization chemistry, we also functionalized the unclad portion of the optical fibers to construct the FO-PPR sensor. A microfluidic chip was integrated with the FO-PPR sensor. This FO-PPR sensor is sensitive to the refractive index of the surrounding medium of the AuNPs on the fiber. The RIR of the FO-PPR
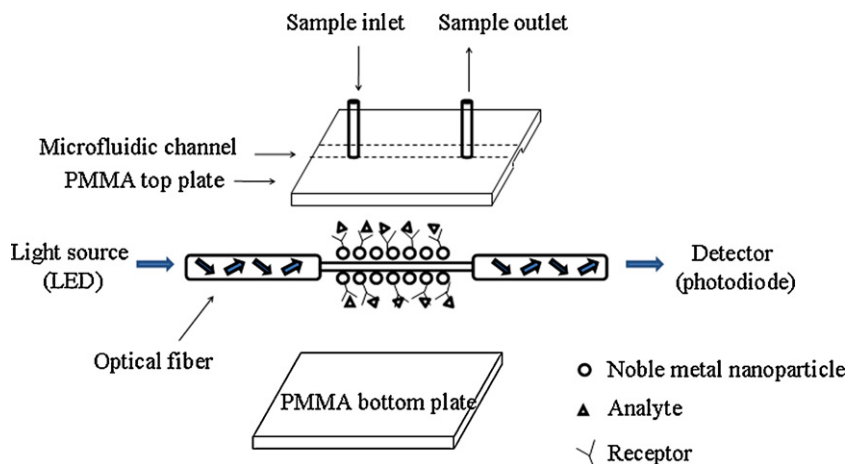
Fig. 1. Schematic representation of the components used for the FO-PPR microfluidic sensor chip. A sensor fiber is placed into the microfluidic channel on the top plate and caped with the bottom plate.
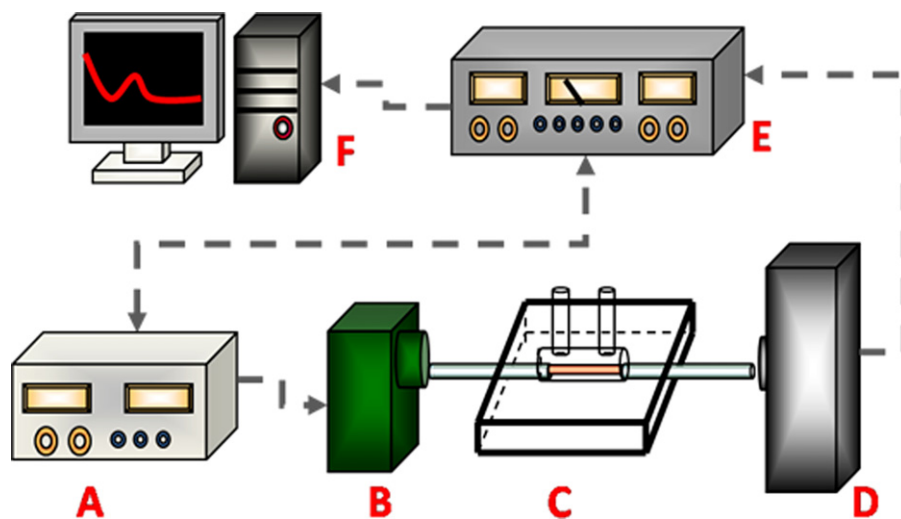
Fig. 2. Schematic representation of the setup used for the FO-PPR sensor system. The setup consists of: A, function generator; B, light-emitting diode; C, FO-PPR sensor chip; D, photodiode; E, lock-in amplifier; F, computer.
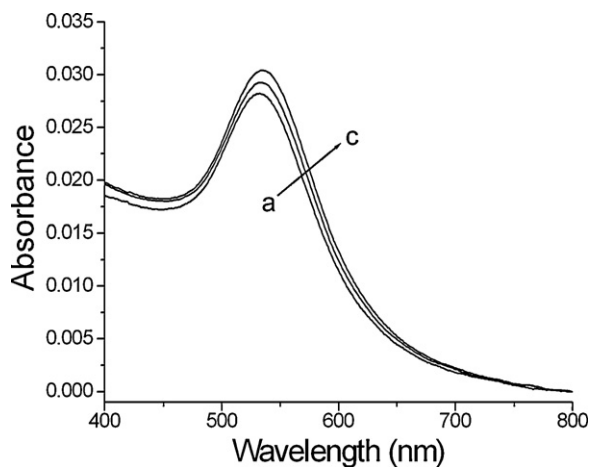

Fig. 3. Absorbance spectra of a monolayer of AuNPs on glass: (a) without treatment; (b) with biotin-functionalization; (c) after the biotin-functionalized gold nanoparticle monolayer immersed in a solution of anti-biotin (1×10^{-5} M). All spectra were obtained in air.

sensor in the microfluidic flow-cell was 2.9×10^{-5} RIU while a similar FO-PPR sensor in a conventional cell had a RIR of 7.0×10^{-5} RIU. Such a comparison indicates that the RIR improves 2.4-fold when the FO-PPR sensor is integrated with the microfluidic flow-cell. With a further improvement in photonics and electronics, a RIR of 1.9×10^{-6} RIU has been achieved [33]. Although some SPR sensors have demonstrated a RIR better than 1×10^{-7} RIU [6], Van Duyne and coworkers have demonstrated that the SPR and PPR sensors are comparable in their sensitivities when measuring short-range changes in RI owing to a molecular adsorption layer [44]. This is a result of the much smaller sensing volume offered by the PPR sensors (20−40 nm) [45,46], as the electromagnetic field decay length is about 10 times shorter than that of the SPR sensors (200−400 nm) [47].

In this study, the conventional cell was a rectangular cell with a volume of 3 mL. When sucrose solutions of different refractive indexes were loaded into the conventional liquid cell, we had to suck the solution in the cell by a dropper first and load a new solution with a higher refractive index into the cell. Carryover is one of the most commonly encountered problems for conventional liquid cells. On the other hand, the microfluidic flow-cell is very narrow and its free volume is only about 14 μL. Thus, the cell can be filled quickly and completely with a sample of very small volume.
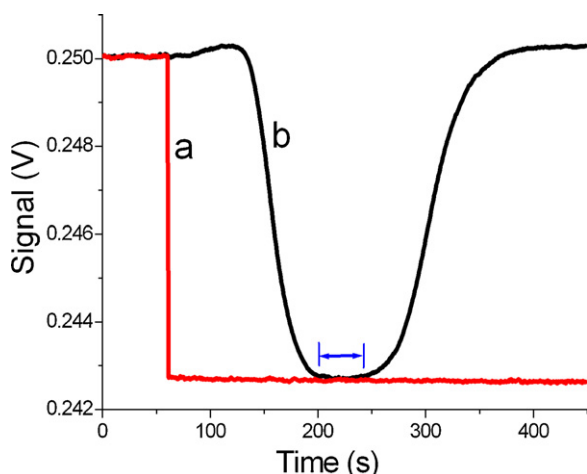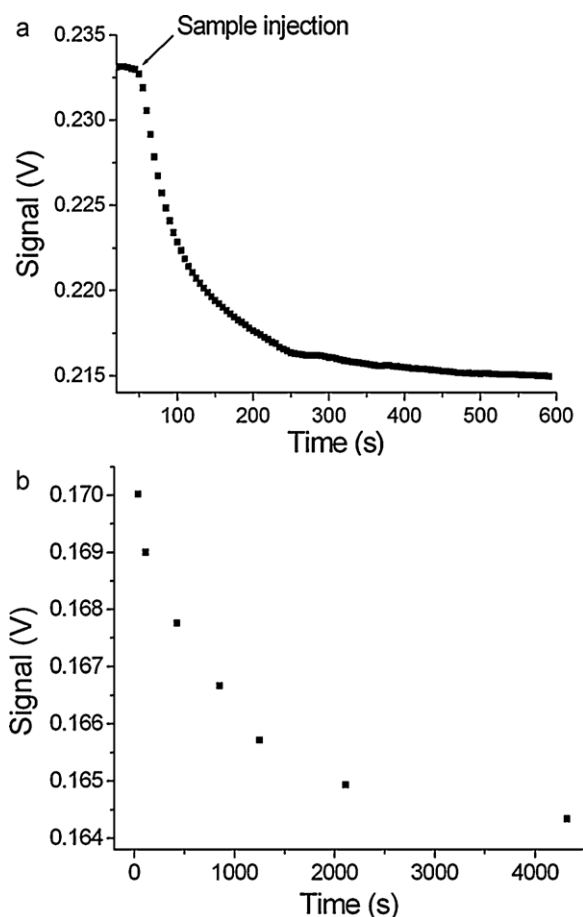
Fig. 4. Temporal sensor responses obtained by the microfluidic FO-PPR sensor chip when (a) a large sample of sucrose solution (6.8%) was directly injected into the cell and (b) 100 μL of sucrose solution (6.8%) was injected into the cell via a sample injector and an inlet tubing (20 cm). A flow rate of 50 μL mL^{-1} was used for both injections. The zone with dispersion of unity is defined as the zone where the signal change is greater than 99% of the signal change shown by curve a.

Although band dispersion in flow-injection systems may cause dilution of samples, the dispersion becomes unity when the sample volume is just several-fold larger than the cell volume. Fig. 4 shows the sensorgrams obtained by the microfluidic FO-PPR biosensor system in two different conditions. Curve a of Fig. 4 was obtained when a large sample of sucrose solution was directly injected into the microfluidic flow-cell without passing through an inlet tube while Curve b of Fig. 4 was obtained when 100 μL of sucrose solution was injected into the microfluidic flow-cell through a sample injection valve and an inlet tube. With a flow rate of 50 μL min^{-1} as shown in Curve b of Fig. 4, a zone with dispersion of unity exists and it has a volume of about 34 μL, which is greater than the free volume of the flow-cell. Under these conditions, no appreciate mixing of sample and carrier takes place, and thus no sample dilution occurs. The volume of the zone without dispersion in general can be increased by using a shorter tube and/or a lower flow rate. Since the carryover effect is negligible with a microfluidic flow-cell, the RIR of the FO-PPR with microfluidic flow-cell improves as compared to that with the conventional liquid cell.

3.3. Response time

One of the advantages of a label-free biosensor is its capability of real-time detection of biomolecular interactions. Fig. 5a depicts a microfluidic FO-PPR sensorgram of a solution of anti-DNP (6.0 × 10^{-6} M) injected over a surface with immobilized DNP as a receptor. Before injection of the sample, the baseline stability was assured by having a drift of $\Delta I/I_0 < 0.094\%$ in the PBS solution. Incubation of the sensor surface with the anti-DNP sample resulted in a dramatic, time-dependent decrease in sensor response since the antigen–antibody interaction led to a local increase of refractive index near the gold nanoparticle surface and, hence, an increase in absorbance at 530 nm and a decrease in light intensity at the detector. The real-time response shows that the microfluidic FO-PPR sensor requires more than 4.0 × 10^2 s to reach a steady-state response and the response time (t_{95}, time to reach 95% of the equilibrium signal level) is 2.94 × 10^2 s. On the other hand, the FO-PPR sensor in the conventional liquid cell requires more than 4 × 10^3 s to reach a steady-state response and the response time is 2.72 × 10^3 s, as shown in Fig. 5b. Thus, integration of the FO-PPR sensor with the microfluidic flow-cell results in a significantly reduced response

Fig. 5. Temporal sensor responses obtained by a DNP-functionalized FO-PPR sensor in (a) microfluidic flow-cell and (b) conventional liquid cell. Anti-DNP of 6.0 × 10^{-6} M was used as the sample.

time from several thousand seconds in the conventional liquid cell to several hundred seconds in the microfluidic flow-cell.

The reduction in response time can be accounted for by an expression derived from the Fick's Law of Diffusion [3]:

$$T = \frac{L^2}{D}$$

where T, L, and D are the molecular transportation time, diffusion distance, and diffusion coefficient, respectively. This means that a down-scale to 1/10 of the original size of the sensing cell reduces the molecular transport time to 1/100 [48]. Based on this relationship, a decrease in the response time by reducing the width of the microfluidic channel is expected. In the present design, the characteristic diffusion distance can be set as half of the distance from the surface of channel to core surface of the optical fiber because the analyte is filled in the channel initially. Therefore, L can be estimated as 125 μm. Assuming a diffusion coefficient of 4 × 10^{-7} cm^2 s^{-1} for antibody [49], the diffusion time is calculated to be 391 s, which is in the same order of magnitude compared to the response time observed here.

The response time is also affected by the diffusion coefficient of the analyte, which is inversely proportional to the effective size of the molecule [50]. The linear size of a molecule generally varies as the cube root of the molecular weight, so that the molecular transportation time or the response time generally also varies as the cube root of the molecular weight. To investigate this effect, we carried out a series of biomolecular interaction analysis using analytes of various molecular weights to determine the corresponding
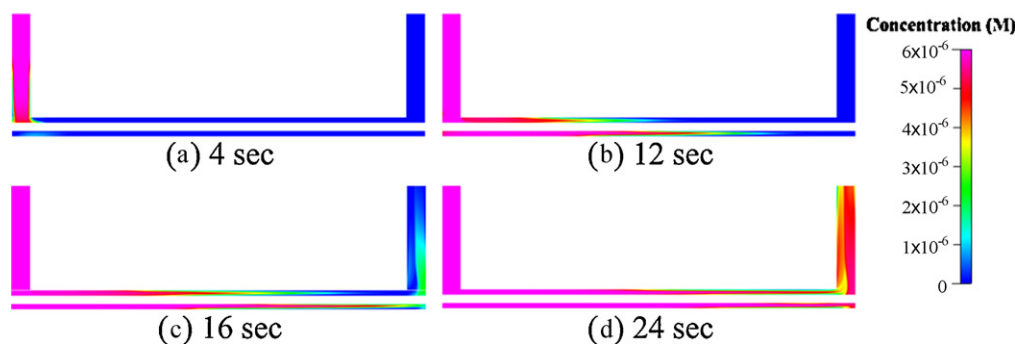
Fig. 6. Simulated concentration profiles during injection of a sample into the microfluidic channel of a FO-PPR sensor chip at (a) 4 s; (b) 12 s; (c) 16 s; and (d) 24 s. The injected volume and flow rate of the sample were fixed at 20 μL and 50 μL min^{-1}, respectively. The injected concentration of the analyte was set as 6 μM. The surface concentration of the receptor was assumed to be 1×10^{-8} mol m^{-2}.

response times. As shown in Table 1, the response time increases when the molecular weight of the analyte increases.

In flow systems, dead volume is always a concern because it will affect fluid exchange and perhaps the response time of a sensor. In the present deign, there is a possibility of having dead volumes in the vicinity of input/output ports of the microfluidic channel. To investigate the issue of dead volume, we carried out simulations for the transient state concentration profiles during sample injection using the CFD-ACE^{TM} software [51]. A fixed-velocity condition was set to the boundary condition at the inlet of the microfluidic channel. The boundary condition at the outlet was set at a fixed pressure. The surface of the optical fiber was set as the reactive boundary for biomolecular binding. The association and dissociation rate constants, k_a and k_d, of the analyte were assumed to be 1.3×10^5 M^{-1} s^{-1} and 6.5×10^{-5} M^{-1} s^{-1}, respectively [52]. The diffusion coefficient of the analyte was assumed to be 4×10^{-7} cm^2 s^{-1} [49].

Fig. 6 reveals the transient distributions of the sample concentration during the injection. With a flow rate of 50 μL min^{-1}, ideally it will take about 17 s to fill the channel. According to the simulation results, there is dead volume in the vicinity of the input port when the sample just reaches the core surface of the optical fiber (time = 4 s). However, the dead volume disappears in 12 s when the flow passes through the corner close to the input port, as shown in Fig. 6b. The similar situation occurs in the vicinity of the output port (time = 16 s) and the dead volume has been filled in 24 s after the sample passed through the corner near the output port. The simulated results indicate that the possible dead volumes are almost eliminated with a sample injection period of 24 s, which is just slightly longer than the ideal sample injection period of 17 s.

3.4. Detection limit

Although in principle a refractive index sensor is almost totally insensitive to volume change of the sensing cell [48], the performance of a biosensor has been suggested to be limited by the rate at which an analyte molecule is transported to a surface-immobilized recognition molecule [1,2]. When this binding process is diffusion limited, the sensor's detection limit and response time are limited by analyte mass transport. For large equilibrium association con-

stant, this fundamental limit has been suggested to be given by a simple scaling relationship [53]:

$$N(t) \approx kC_0 t^{1/F}$$

where $N(t)$ is the total number of adsorbed molecules on sensor surface at time t, k is a constant, C_0 is the concentration of the analyte far from the interface, and F is the fractal dimension of the sensor surface (typically, $1 < F < 2$). Although this expression has not considered the equilibrium sensor response, it should be valid for the early stage of the temporal sensor response. Hence, for any finite measurement time t_s, $N(t)$ grows in time. As the FO-PPR sensor in the conventional liquid cell requires several thousand seconds to reach a steady-state response while the FO-PPR sensor in the microfluidic flow-cell only requires several hundred seconds to reach a steady-state response, using t_s of just several hundred seconds in both cells will result in significantly different $N(t)$ values and hence significantly different detection limits.

The comparison of detection limits for the FO-PPR sensor in the conventional liquid cell and microfluidic flow-cell for 3 analytes with different molecular weights were made. As shown in Table 2, the detection limits for streptavidin, anti-biotin, and anti-DNP under similar conditions improved by about 9-fold, 26-fold, and 33-fold, respectively, when the FO-PPR sensor was integrated with the microfluidic cell. The improvement of detection limit may be attributed to the higher number of adsorbed molecules in a finite measurement time and the negligible carry-over effect in the microfluidic flow-cell. Thus, it can be concluded that biointeraction analysis by the integration of FO-PPR sensor with microfluidic flow-cell requires a shorter analysis time and is more sensitive.

3.5. Selectivity

Besides the high sensitivity of the FO-PPR biosensor, its selectivity is of equal importance. The practical detection limit will be determined by the nonspecific interactions between the noble metal nanoparticles and interfering biomolecules. In order to minimize nonspecific adsorption, an optimized mixed monolayer on

Table 1
Response times of analytes with various molecular weights obtained by the microfluidic FO-PPR sensor chips under similar immobilization and detection conditions. Concentrations of all the analytes were at 6.0×10^{-6} M.

Analyte	Molecular weight (kDa)	Response time, t_{95} (s)
Anti-DNP	220	294
Anti-biotin	150	279
Streptavidin	67	169

Table 2
Comparison of microfluidic flow-cell and conventional liquid cell for determination of refractive index resolution (RIR) and detection limit (DL) by the FO-PPR sensor. The immobilized receptors for the corresponding analytes, anti-DNP, anti-biotin, and streptavidin, were DNP, biotin, and biotin, respectively.

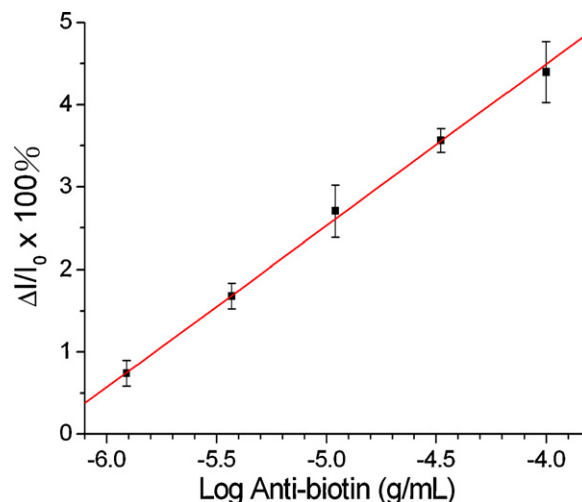| RIR or DL	Microfluidic cell	Conventional cell
RIR	2.9×10^{-5} RIU	7.0×10^{-5} RIU
DL for streptavidin	1.1×10^{-11} M	9.8×10^{-11} M
DL for anti-biotin	3.3×10^{-9} M	8.5×10^{-8} M
DL for anti-DNP	1.2×10^{-12} M	4.0×10^{-11} M
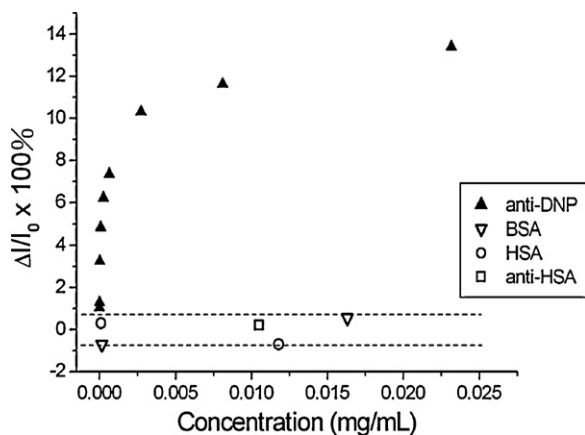
Fig. 7. Sensor responses of a DNP-functionalized FO-PPR sensor in pH 7.2 phosphate buffer solutions containing anti-DNP, anti-HSA, HSA, or BSA of various concentrations. The measurements were taken in a conventional liquid cell by a setup similar to Fig. 2 but without the function generator and lock-in amplifier. The dash lines represent the signal levels, $S = S_b \pm 3\sigma_b$, where S_b is the average sensor response in a blank and σ_b is the standard deviation of the noise in a blank.

Fig. 8. Reproducibility of the microfluidic FO-PPR sensor chips for detection of anti-biotin ($n = 3$). The immobilized receptor was biotin. All sensor responses shown were determined at a concentration above the quantification limit of the sensor.

gold nanoparticle surface as previously reported was used [33]. To verify that the sensor response is the result of specific binding between the analyte molecules and the receptor molecules on the nanoparticle surface, binding tests with anti-DNP, anti-HSA, HSA, or BSA interacting with a DNP-functionalized FO-PPR sensor were performed. Fig. 7 shows that the sensor response increased as the anti-DNP concentration increased due to the specific interaction between DNP and anti-DNP while there was no significant change in sensor response when anti-HSA, HSA, or BSA of various concentrations was added. Thus, an appropriately functionalized FO-PPR sensor can be used to interrogate receptor-analyte binding events with high sensitivity as well good selectivity.

3.6. Reproducibility

As the PMMA microfluidic chips manufactured by the injection molding technique can be easily mass produced, low-cost disposable FO-PPR sensors are possible. To meet analytical performance standards, reproducibility of the chip fabrication processes is important. Our previous study using AuNPs in the FO-PPR biosensor for determination of interleukin-1β (IL-1β) showed that the microfluidic FO-PPR sensor chips had reasonably good measurement reproducibility among 5 different chips, with a coefficient of variation (CV) between 6.7% and 18.7% at 6 different concentrations of IL-1β and the CV decreased as the concentration increased from 0.050 to 10 ng mL^{-1} [33].

This study also investigates the chip-to-chip measurement reproducibility using AgNPs in the FO-PPR biosensor for determination of anti-biotin. Fig. 8 shows a calibration graph of the average sensor response ($\Delta I/I_0$) for 3 different chips versus log anti-biotin concentration using biotin-functionalized AgNPs on the sensor surface. The plot is linear (correlation coefficient, $r = 0.9996$) and a detection limit of 2.1×10^{-9} M and a quantification limit of 3.0×10^{-9} M are estimated. The CVs of the sensor responses at the 5 different concentrations are between 4.0% and 21.1%. Excluding the data point at the lowest concentration, the CVs of the sensor responses are between 4.0% and 11.7%, suggesting the performance of the sensor chips is reasonably reproducible. It should be noted that the I_0 measured in these sensor chips were slightly different (data not shown). However, the normalization by $\Delta I/I_0$, the relative change of transmission response, alleviates the demand on precise optical alignment. We believe an improvement in the fabrication reproducibility of the sensor fibers in terms of the characteris-

tics of the noble metal nanoparticles such as size distribution and coverage should further improve the chip-to-chip measurement reproducibility.

3.7. Reusability

The regeneration of immobilized receptor is of major importance for re-usable sensor formats. Fig. 9 demonstrates the overall stability of immobilized OVA and the sensor chip through 3 binding–regeneration cycles without loss of surface binding capacity. A consistent anti-OVA binding level (CV = 3.6%) is maintained through at least 3 binding–regeneration cycles (the maximum number we tested) and regeneration gives a stable baseline (CV = 2.4%) throughout the analysis. Furthermore, these sensor chips in the absence of immobilized receptor have a storage lifetime (under ambient condition) of at least 2 months (the maximum time tested) without affecting the reproducibility of the results.
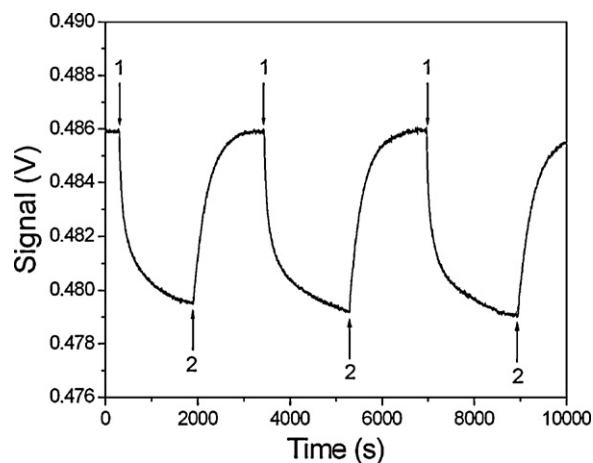
Fig. 9. Binding and regeneration response of 3 binding-regeneration cycles for the interaction between immobilized OVA and anti-OVA at 25 °C. Arrow 1 indicates injection of anti-OVA solution (6.25×10^{-5} g mL^{-1}) and arrow 2 indicates injection of regeneration solution (10 mM glycine–HCl, pH 1.8). The sensorgram was obtained in a microfluidic chip with a channel dimension larger than that described in the experimental section.

Table 3
Concentration of MMP-3 measured in synovial fluid samples from 6 osteoarthritis patients by FO-PPR and ELISA methods.

Sample	MMP-3 concentration (Mean ± SD) in synovial fluid ($n = 3$)	
	By FO-PPR (pM)	By ELISA (pM)
No. 1	127 ± 2.3	144 ± 13.0
No. 2	84 ± 0.8	102 ± 2.0
No. 3	97 ± 1.4	96 ± 4.8
No. 4	81 ± 3.6	82 ± 1.1
No. 5	118 ± 3	98 ± 5.8
No. 6	192 ± 3.7	183 ± 2.0

3.8. Validation in real samples

To validate the FO-PPR biosensor chip in real samples, this sensing strategy was used for the quantitative analysis of matrix metalloproteinases-3 (MMP-3) in synovial fluid and compared with the results by ELISA using the same set of samples. Matrix metalloproteinases are enzymes involved in the degradation of cartilage matrix components [54]. MMP-3 has been detected in synovial fluid from osteoarthritis patients [55] and the relationship between severity of cartilage damage and synovial activity of matrix metalloproteinases has been shown [56]. Table 3 shows the concentrations of MMP-3 of 6 synovial fluid samples obtained by the FO-PPR sensor and the ELISA method. The paired t-test indicates that the mean of the differences between the data of the two groups does not differ significantly from zero ($P = 0.8747$). The data passed the normality test with $P > 0.05$. In other words, there is no significant difference between each pair of results by the two methods.

4. Conclusion

In this research, we have successfully demonstrated the integration of the FO-PPR biosensor with a microfluidic chip. With either AuNPs or AgNPs used in the sensor fiber, the chip-to-chip measurement reproducibility is reasonably good. Since the principle of FO-PPR measurements is based on absorption spectroscopy, the need for precise optical alignments is alleviated. In other words, the FO-PPR sensor response presented as $(I_0 - I_S)/I_0$ or $\Delta I/I_0$ provides a mean of normalization to ensure that some variation of I_0 is acceptable. Together with the simple instrumental setup, the FO-PPR biosensing system is potentially a low-cost and portable biosensor candidate compared to the bulky and more expensive commercial instruments.

References

[1] P.E. Sheehan, L.J. Whitman, Nano Letters 5 (2005) 803–807.
[2] P.R. Nair, M.A. Alam, Appl. Phys. Lett. 88 (2006) 233120.
[3] K. Sato, A. Hibara, M. Tokeshi, H. Hisamoto, T. Kitamori, Adv. Drug Deliv. Rev. 55 (2003) 379–391.
[4] C. Phillips, M. Jakusch, H. Steiner, B. Mizaikoff, A.G. Fedorov, Anal. Chem. 75 (2003) 1106–1115.
[5] T. Gervais, K.F. Jensen, Chem. Eng. Sci. 6 (2006) 1102–1121.
[6] J. Homola, Chem. Rev. 108 (2008) 462–493.
[7] C.E.H. Berger, T.A.M. Beumer, R.P.H. Kooyman, J. Greve, Anal. Chem. 70 (1998) 703–706.
[8] H.J. Lee, T.T. Goodrich, R.M. Corn, Anal. Chem. 73 (2001) 5525–5531.
[9] B.P. Nelson, A.G. Frutos, J.M. Brockman, R.M. Corn, Anal. Chem. 71 (1999) 3928–3934.
[10] B. Rothenhausler, W. Knoll, Nature 332 (1988) 615–617.
[11] B.P. Nelson, T.E. Grimsrud, M.R. Liles, R.M. Goodman, R.M. Corn, Anal. Chem. 73 (2001) 1–7.
[12] G.J. Wegner, N.J. Lee, G. Marriott, R.M. Corn, Anal. Chem. 75 (2003) 4740–4746.
[13] E.A. Smith, W.D. Thomas, L.L. Kiessling, R.M. Corn, J. Am. Chem. Soc. 125 (2003) 6140–6148.
[14] V. Kanda, J.K. Kariuki, D.J. Harrison, M.T. McDermott, Anal. Chem. 76 (2004) 7257–7262.
[15] R.C. Jorgenson, S.S. Yee, Sens. Actuat. B 12 (1993) 213–220.
[16] J. Homola, R. Slavik, Electron. Lett. 32 (1996) 480–482.
[17] L.A. Obando, K.S. Booksh, Anal. Chem. 71 (1999) 5116–5122.
[18] N.L. Rosi, C.A. Mirkin, Chem. Rev. 105 (2005) 1547–1562.
[19] J.A. Anker, W.P. Hall, O. Lyandres, N.C. Shan, J. Zhao, R.P. Van Duyne, Nat. Mater. 7 (2008) 442–453.
[20] M.E. Stewart, C.R. Anderton, L.B. Thompson, J. Maria, S.K. Gray, J.A. Rogers, R.G. Nuzzo, Chem. Rev. 108 (2008) 494–521.
[21] P. Mulvaney, Langmuir 12 (1996) 788–800.
[22] T.R. Jensen, M.L. Duval, K.L. Kelly, A.A. Lazarides, G.C. Schatz, R.P. Van Duyne, J. Phys. Chem. B 103 (1999) 9846–9853.
[23] Y. Sun, Y. Xia, Anal. Chem. 74 (2002) 5297–5305.
[24] E.M. Larsson, J. Alegret, M. Kall, D.S. Sutherland, Nano Letters 7 (2007) 1256–1263.
[25] H. Chen, X. Kou, Z. Yang, W. Ni, J. Wang, Langmuir 24 (2008) 5233–5237.
[26] C.D. Chen, S.F. Cheng, L.K. Chau, C.R.C. Wang, Biosens. Bioelectron. 22 (2007) 926–932.
[27] P. Englebienne, Analyst 123 (1998) 1599–1603.
[28] A.J. Haes, R.P. Van Duyne, J. Am. Chem. Soc. 124 (2002) 10596–10604.
[29] N. Nath, A. Chilkoti, Anal. Chem. 74 (2002) 504–509.
[30] S.F. Cheng, L.K. Chau, Anal. Chem. 75 (2003) 16–21.
[31] S.F. Cheng, L.K. Chau, K.C. Pao, J. Biomed. Nanotechnol. 1 (2005) 143–150.
[32] L.K. Chau, Y.F. Lin, S.F. Cheng, T.J. Lin, Sens. Actuat. B 113 (2006) 100–105.
[33] C.Y. Chiang, M.L. Hsieh, K.W. Huang, L.K. Chau, C.M. Chang, S.R. Lyu, Biosens. Bioelectron. 26 (2010) 1036–1042.
[34] N.S. Lai, C.C. Wang, H.L. Chiang, L.K. Chau, Anal. Bioanal. Chem. 388 (2007) 901–907.
[35] V.V.R. Sai, T. Kundu, S. Mukherji, Biosens. Bioelectron. 24 (2009) 2804–2809.
[36] X.D. Hoa, A.G. Kirk, M. Tabrizan, Biosens. Bioelectron. 23 (2007) 151–160.
[37] C. Huang, K. Bonroy, G. Reekmans, W. Laureyn, I. De Vlaminck, L. Lagae, G. Borghs, Biomed. Microdevices 11 (2009) 893–901.
[38] C.H. Chen, T.C. Tsao, W.Y. Li, W.C. Shen, J.L. Tang, C.P. Jen, C.W. Cheng, L.K. Chau, W.T. Wu, Microsyst. Technol. 16 (2010) 1207–1214.
[39] P.Y. Silvert, H.U. Ronaldo, E.T. Kamar, J. Mater. Chem. 7 (1997) 293–299.
[40] S.K. Khijwania, B.G. Gupta, Opt. Commun. 152 (1998) 259–262.
[41] P.H. Paul, G. Kychakoff, Appl. Phys. Lett. 51 (1987) 12–14.
[42] H. Tai, H. Tanaka, T. Yoshino, Opt. Lett. 12 (1987) 437–439.
[43] S.A. Merschman, D.C. Tilotta, Appl. Spectrosc. 52 (1998) 106–111.
[44] D.A. Stuart, A.J. Haes, C.R. Yonzon, E.M. Hicks, R.P. Van Duyne, IEE Proc. Nanobiotechnol. 152 (2005) 13–32.
[45] D.D. Evanoff Jr., R.L. Ryan, G. Chumanov, J. Phys. Chem. B 108 (2004) 1522–1528.
[46] N. Nath, A. Chilkoti, Anal. Chem. 76 (2004) 5370–5378.
[47] J. Homola, S.S. Yee, G. Gauglitz, Sens. Actuat. B 54 (1999) 3–15.
[48] A. Manz, N. Graber, H.M. Widmer, Sens. Actuat. B 1 (1990) 244–248.
[49] D.A. Berk, F. Yuan, M. Leunig, R.K. Jain, Biophys. J. 65 (1993) 2428–2436.
[50] J.P. Brody, P. Yager, R.E. Goldstein, R.H. Austin, Biophys. J. 71 (1996) 3430–3441.
[51] C.T. Huang, C.P. Jen, T.C. Chao, W.T. Wu, W.Y. Li, L.K. Chau, Sensors 9 (2009) 6456–6470.
[52] K.M. Mayer, S. Lee, H. Liao, B.C. Rostro, A. Fuentes, P.T. Scully, C.L. Nehl, J.H. Hafner, ACS Nano 2 (2008) 687–692.
[53] P.R. Nair, M.A. Alam, Phys. Rev. Lett. 99 (2007) 256101.
[54] D.D. Dean, J. Martel-Pelletier, J.P. Pelletier, D.S. Howell, J.F. Woessner, J. Clin. Invest. 84 (1989) 678–685.
[55] N. Ishiguro, T. Ito, H. Ito, H. Iwata, H. Jugessur, M. Ionescu, A.R. Poole, Arthritis Rheum. 42 (1999) 129–136.
[56] M. Maiotti, G. Monteleone, U. Tarantino, G.F. Fasciglione, S. Marini, M. Coletta, Arthroscopy 16 (2000) 522–526.